Available online at www.sciencedirect.com

ScienceDirect

Acta Materialia 77 (2014) 1–16

Acta MATERIALIA

www.elsevier.com/locate/actamat

The effect of Mn and Zr dispersoid-forming additions on recrystallization resistance in Al–Cu–Li AA2198 sheet

D. Tsivoulas *, P.B. Prangnell

School of Materials, The University of Manchester, Manchester M13 9PL, UK

Received 14 February 2014; received in revised form 8 May 2014; accepted 17 May 2014
Available online 24 June 2014

Abstract

The influence of sole and joint Zr and Mn additions on the recrystallization behaviour of an AA2198-base alloy has been compared during extended annealing at 535 °C, following hot rolling to sheet. With a constant Zr level recrystallization resistance was seen to diminish with the addition of Mn and became progressively worse with a decrease in Zr content, as more Mn was added. It has been found that this behaviour arises because the additional pinning pressure of $Al_{20}Cu_2Mn_3$ dispersoids does not adequately compensate for the expansion in width of the Al_3Zr-free bands that occurs on the addition of Mn to the base alloy, even with the same Zr level. The lower potency of Mn, relative to Zr, in inhibiting recrystallization has been attributed to the poorer coherency and higher aspect ratio of the $Al_{20}Cu_2Mn_3$ dispersoids, which reduces their Zener pinning pressure by a factor of four relative to that of the Al_3Zr phase. In addition, the presence of the coarser $Al_{20}Cu_2Mn_3$ dispersoids was found to increase the stored energy after hot rolling. The recrystallization mechanism was dependent on the dispersoid type. The addition of Zr led to the dominance of broad front strain-induced boundary migration (SIBM), whereas the addition of Mn-containing dispersoids favoured particle-stimulated nucleation (PSN). Texture measurements have verified this observation, with SIBM favouring the growth of recrystallized grains of orientations typical of the deformation texture and PSN promoting the growth of randomly orientated grains during recrystallization.

Keywords: Recrystallization; Dispersoids; Al–Li alloys; Stored energy; Zener pinning

1. Introduction

The demand for better damage tolerance in advanced Al–Cu–Li alloys has revived interest in obtaining a more complete understanding of the role that dispersoid-forming alloy additions perform in these alloys [1]. This enhanced interest stems from the fact that dispersoids play an important role in preventing recrystallization during solution treatment and because partially recrystallized microstructures exhibit inferior fracture toughness, compared to fully fibrous grain structures [2–9]. The joint addition of Zr and Mn dispersoid-forming elements has been introduced relatively recently to plate products, such as AA2050 [10–12]. The rationale behind the combined addition of Mn and Zr is based on the opposite microsegregation patterns these elements form during casting [13,14]. In theory, this should increase recrystallization resistance by leading to a greater uniformity of dispersoid coverage [15–19], consequently improving fracture toughness [20–22]. However, in recent work on AA2198 alloy sheet by the present authors [14,23,24], a subtle interaction was observed between Zr and Mn when the latter element was added to the baseline alloy, which resulted in a reduction in recrystallization resistance.

It is well known that in commercial Al–Cu–Li alloys the addition of Zr leads to the precipitation of the metastable β′-Al_3Zr phase during homogenization treatments [25].

* Corresponding author. Tel.: +44 1613068959.
E-mail address: dimitrios.tsivoulas@manchester.ac.uk (D. Tsivoulas).

http://dx.doi.org/10.1016/j.actamat.2014.05.028
1359-6454/

This phase typically forms as fine spherical dispersoids that are coherent with the Al matrix [26]. In comparison, Mn forms larger, semicoherent, lath-shaped $Al_{20}Cu_2Mn_3$ dispersoids [27]. The size, number density, distribution and morphology of these dispersoids depends strongly on the homogenization treatment and local supersaturation in the cast microstructure [28,29]. Because Zr and Mn have opposing microsegregation patterns in aluminium (arising from partition coefficients of >1 and <1, respectively [30,31]), β′ is typically found to precipitate within the dendrite cores and the $Al_{20}Cu_2Mn_3$ dispersoids are concentrated towards the dendrite/grain boundaries. These two families of dispersoids are consequently found to have a banded distribution (in the normal direction (ND)) in rolled products, with layers between the bands containing a low dispersoid density of the two respective dispersoid types [23].

In a recent previous study [23] it was found that addition of Mn to an AA2198 alloy containing 0.11 wt.% Zr resulted in the average number density of the Al_3Zr dispersoids being reduced and their size slightly increased. However, a more important influence was found on the width of the low Al_3Zr particle density bands seen in sheet material. This behaviour was shown to be caused by a small amount of Zr being dissolved into the Mn-bearing phases, which had a disproportionate effect on Al_3Zr precipitation in the interdendritic regions in the cast billet, where there was already a low Zr supersaturation. However, in this work the dominant recrystallization mechanisms operating in the materials and the effect of the two different dispersoid types on their texture development were not investigated.

The presence of two dispersoid families that form alternating bands in the ND in a rolled sheet is likely to interact in a complex manner with any recrystallization front that forms on annealing. In hot-rolled aerospace alloys the main mechanisms of recrystallization are generally found to be particle-stimulated nucleation (PSN), when new grains grow from the deformation zones around coarse constituent particles located at prior grain boundaries that are associated with a low dispersoid density [32–39]; and strain-induced boundary migration (SIBM), which takes place by the migration of a pre-existing high-angle grain boundary (HAGB) into a region of higher stored energy [32–34,40–44]. Both of these mechanisms are strongly dependent on the presence of pinning particles. The effect of pinning particles on PSN is to increase the critical size of the nucleus [32] and on SIBM to retard grain boundary mobility, which can favour broad front SIBM [45,46]. The recrystallization mechanism can also affect the recrystallization texture, through influencing the growth or consumption of specific texture components [32,33,45,47–54].

Although the effect of dispersoid particles on the recrystallization resistance of aluminium alloys has been extensively investigated [32,47–49,55–57], currently no work in the literature has investigated in detail the mechanisms of recrystallization operating when dual $Al_{20}Cu_2Mn_3$ and Al_3Zr dispersoid phases are present in commercial Al–Cu–Li alloys. The scope of the present work was to address this issue by systematically comparing the recrystallization behaviour of an AA2198 base alloy, containing individual and joint Al_3Zr and $Al_{20}Cu_2Mn_3$ dispersoid phases. The effect of the dispersoid additions on the texture evolution is also discussed.

2. Experimental

The materials used in this study were supplied by Constellium, Centre de Recherches de Voreppe, France, in the form of 6 mm thick sheet, with two different temper conditions; hot-rolled (F temper), and solution-treated, stretched and naturally aged (T351 temper). The production route involved direct chill (DC) casting, homogenization, and hot rolling down to the final gauge, for which the total true strain was ~4. The experimental alloys were based on the composition of AA2198, and were produced with both individual and joint combinations of the dispersoid-forming elements Zr and Mn. The alloy compositions and designations are presented in Table 1. Although the exact composition has not been given for the Cu, Li, Mg, and Ag levels, great care was taken in ensuring tight composition control, with variability between castings kept to <3% for each element. However, the Zr and Mn levels provided in Table 1 are actual values measured from chemical analysis. The experimental alloys underwent a standard single-temperature homogenization treatment. Unfortunately, at the time of the research the 2198–0.1Zr alloy was not available in the F temper with the same homogenization treatment and an otherwise identical sample that had been subjected to a two-stage homogenization was consequently included in the study. This alloy has been labelled 2198–0.1Zr-D, so that it can be distinguished from the alloy with the standard treatment.

Isothermal annealing treatments were carried out on the samples, in both the F and T351 tempers, at the solution treatment temperature of 535 °C followed by quenching in water. Microstructural analysis was carried out by means of scanning electron microscopy plus electron backscatter diffraction (SEM/EBSD) and transmission electron microscopy (TEM) on samples cut from rolling direction (RD)–ND cross-sections after different annealing times. An FEI Sirion FEG-SEM with an EBSD system was used to characterize the grain structures, textures and the volume fraction of recrystallization on samples that were metallographically prepared followed by light electropolishing. Several hundred grains were measured in each condition. An FEI Tecnai FEG-TEM operating at 300 kV was used to analyze the microstructures in more detail and measure the dispersoid and subgrain sizes more accurately. Subgrain sizes were measured by the linear intercept method in accordance with ASTM E 562-02 [58]. To quantify the dispersoid number densities and volume fractions, the thickness of the TEM foils was measured with the aid of electron energy loss spectroscopy (EELS)

Table 1
Alloy compositions used in this study (wt.%). The Zr and Mn concentrations were directly measured, whereas, for commercial reasons, the nominal compositions are given for other elements.

Alloy	Cu	Li	Mg	Ag	Zn	Fe	Si	Zr	Mn
2198–0.1Zr	2.90–3.50	0.80–1.10	0.25–0.80	0.10–0.50	<0.08	<0.10	<0.08	0.110	–
2198–0.1Zr–0.3Mn								0.111	0.30
2198–0.05Zr–0.3Mn								0.053	0.31
2198–0.4Mn								–	0.40

by determining the mean free path for energy loss [37,38]. Particle size measurements were carried out in scanning transmission mode (STEM) using a high-angle annular dark field detector (HAADF), in order to take advantage of the atomic number contrast.

The EBSD orientation data was analyzed using the in-house software Vmap (developed by Humphreys [59]), for quantification of the texture. Ideal orientations were defined with a radius of 15°. The misorientation cut-off level selected for high-angle grain boundaries (HAGBs) in the EBSD maps was 15°, while low-angle boundaries (LAGBs) were defined between 15° and 1.5°. Pole figures were plotted with the commercial software HKL CHANNEL5 (Oxford Instruments).

3. Results

3.1. Average dispersoid densities

As will be seen below, the microstructures and texture developed during annealing were strongly influenced by the dispersoid content of the alloys. Measurements of the size and density of the dispersoid particles observed in each alloy in the T351 temper are given in Table 2. Example images of their typical size and distribution can be found in Refs. [14,23]. Following solution treatment, the average diameter of the Al_3Zr dispersoids was smallest in the 2198–0.1Zr base alloy, at 18.8 nm, and increased to 21.3 and 25.3 nm in the 2198–0.1Zr–0.3Mn and 2198–0.05Zr–0.3Mn alloys respectively, while their number density reduced from 252 μm^{-3} in the 2198–0.1Zr baseline material to 174 μm^{-3} in the 2198–0.1Zr–0.3Mn alloy. In contrast, the $Al_{20}Cu_2Mn_3$ dispersoids had a much greater average size and lower number density, which stayed relatively constant in size (~160 nm) but increased in density from 2.6 to 3.6 μm^{-3}, in the alloys containing 0.3 wt.% Mn (2198–0.1Zr–0.3Mn and 2198–0.05Zr–0.3Mn) to the 2198–0.4Mn alloy with 0.4 wt.% Mn.

The relative average boundary pinning pressure, P_z, provided by the dispersoids in each of the 2198 alloy variants was also assessed by comparing the Zener ratio (f_v/r) which is derived from the well-known relationship:

$$P_z^s = \frac{\alpha \gamma f_v}{r}, \quad (1)$$

where α is a numerical constant largely dependent on geometry (ideally = 1.5 for spherical particles), γ is the grain boundary energy, f_v is the particle's volume fraction and r is its radius [60]. Values for f_v/r have been determined separately for the Al_3Zr and $Al_{20}Cu_2Mn_3$ dispersoids within each material, using the equivalent circular diameter for the Mn dispersoids. From this data it can be seen that the 2198–0.1Zr baseline alloy, which contained only Al_3Zr dispersoids, had a f_v/r ratio of 0.093 μm^{-1}. In comparison,

Table 2
Measured size and number density of the Al_3Zr and $Al_{20}Cu_2Mn_3$ dispersoids in the T351 temper.

	2198–0.1Zr-D	2198–0.1Zr	2198–0.1Zr–0.3Mn	2198–0.05Zr–0.3Mn	2198–0.4Mn
Size (nm)					
$Al_{20}Cu_2Mn_3$ length	–	–	233.0 ± 4.0	264.6 ± 7.6	221.7 ± 4.0
$Al_{20}Cu_2Mn_3$ width	–	–	102.8 ± 0.8	107.6 ± 1.2	107.9 ± 0.8
$Al_{20}Cu_2Mn_3$ (ECD)	–	–	152.4	166.2	157.0
Al_3Zr diameter	33.9 ± 0.5	18.8 ± 0.2	21.3 ± 0.3	25.3 ± 0.8	–
Number density (μm^{-3})					
$Al_{20}Cu_2Mn_3$	–	–	2.6 ± 0.2	2.6 ± 0.2	3.6 ± 0.2
Al_3Zr	102 ± 11	252 ± 60	174 ± 23	N/M	–
Interparticle spacing (nm)					
$Al_{20}Cu_2Mn_3$	–	–	402.3	402.3	361.5
Al_3Zr	118.8	87.8	99.2	N/M	–
Volume fraction (10^{-4})					
$Al_{20}Cu_2Mn_3$	–	–	54 ± 3	75 ± 8	94 ± 5
Al_3Zr	20.8 ± 2.3	8.8 ± 2.1	8.8 ± 1.2	N/M	–
f_v/r (μm^{-1})					
$Al_{20}Cu_2Mn_3$	–	–	0.071	0.090	0.120
Al_3Zr	0.123	0.093	0.083	N/M	–

N/M: not measured.

the net average f_v/r ratio determined for the 2198–0.1Zr–0.3Mn alloy, by summing the effect of both types of dispersoids, was the highest of all the materials at 0.150 μm^{-1}, while the 2198–0.4Mn alloy had a f_v/r ratio greater than that of the standard 2198 alloy of 0.120 μm^{-1} owing to its high volume fraction of $Al_{20}Cu_2Mn_3$ particles.

3.2. Stored energy

The energy available for recrystallization in aluminium alloys after hot rolling is largely stored in the form of subgrain boundaries. Subgrain size measurements were carried out by EBSD and TEM on the as-rolled F temper and T351 materials (Fig. 1). The HAADF-STEM images in Fig. 2a–c illustrate the surprisingly large decrease in subgrain size that was observed in the Mn-containing alloys, relative to the baseline alloy with only Zr. Although the 2198–0.1Zr F temper material (2198–0.1Zr-D) unfortunately had experienced a different homogenization treatment, which gave rise to a coarser distribution of Al_3Zr particles than the standard 2198–0.1Zr material, this effect was still clearly seen in unrecrystallized areas of the T351 temper material that had undergone the standard homogenization treatment (2198–0.1Zr), shown in Fig. 2d–f. For example, the alloy containing only Zr had a LAGB ND spacing of ~2 μm, whereas the Mn addition significantly decreased the ND spacing to ~1 μm, in the 2198–0.1Zr–0.3Mn alloy, and was also smaller, but less so, in the 2198–0.05Zr–0.3Mn alloy. It should further be noted that the subgrain morphology had a lower aspect ratio in the Mn-containing alloys (Fig. 1a).

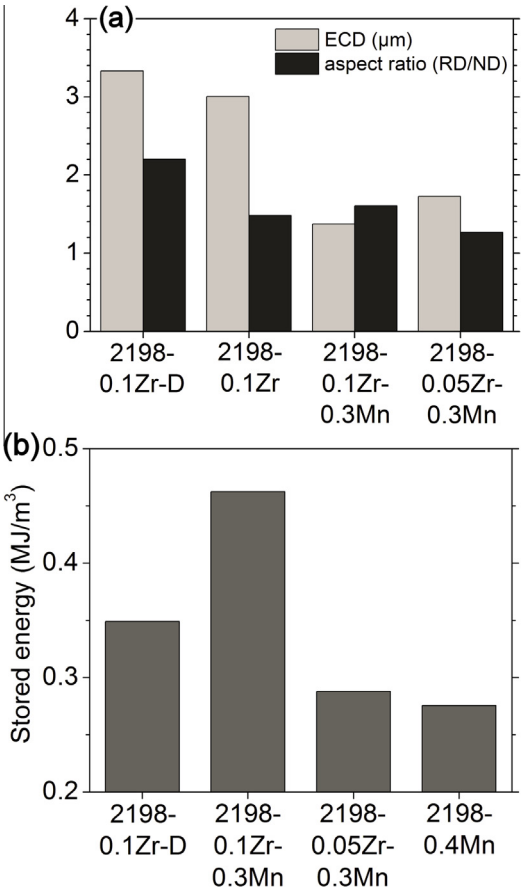

Fig. 1. Substructure characteristics for the AA2198 alloy variants: (a) average subgrain size (ECD) and aspect ratio in the T351 condition (TEM measurements); and (b) calculated average stored energy in the as-hot rolled F temper (EBSD measurements).

Estimates have been made of the stored energy in each material, U_{sg}, using the following relationship:

$$U_{sg} \approx \frac{3\gamma_{HAB}}{d}\frac{\theta}{\theta_m}\left(1 - \ln\frac{\theta}{\theta_m}\right), \quad (2)$$

where θ is the average boundary misorientation and γ_{HAB} is the energy for a non-special high angle boundary, where the cut-off, θ_m, is taken as 15° [32]. Values of the average misorientations of the LAGBs present, θ, and the equivalent subgrain circular diameter, d, were obtained from EBSD orientation maps. Although such estimates of stored energy are not very accurate, the effect of a smaller subgrain diameter on the relative stored energy available for recrystallization is important and Eq. (2) predicts that the 2198–0.1Zr–0.3Mn alloy would have ~30% higher stored energy than the 2198–0.1Zr alloy after hot rolling and prior to annealing (Fig. 1b).

3.3. Grain structure in the T351 solution-treated condition

In industrial practice the final grain structure of an aerospace product is developed in the solution treatment stage prior to artificial aging. The effect of the different dispersoid additions on recrystallization resistance will therefore be first compared in the standard T351 temper. EBSD maps showing the grain structures and levels of recrystallization present in the different materials after solution treatment are provided in Fig. 3 and the area fractions of recrystallization are summarized in Fig. 4a. The alloys that were partially recrystallized exhibited heterogeneous microstructures consisting of regions of fibrous grains elongated along RD, containing well-recovered subgrains, and regions of recrystallized grains that were also highly elongated in RD. Some grains exceeded 1 mm in length, rendering the quantification of their aspect ratio difficult. However, the HAGB ND spacing could be reliably determined from EBSD maps and is presented in Fig. 4b.

It can be clearly seen from Figs. 3 and 4a that the addition of Mn, together with lowering the Zr content, led to a sharp increase in the recrystallized volume fraction, which was nearly zero at the sheet centre for the baseline 2198–0.1Zr alloy and increased to 100% in the 2198–0.4Mn alloy. The overall level of recrystallization increased in order from ~1.5% in the 2198–0.1Zr baseline alloy, to 14% in the 2198–0.1Zr–0.3Mn alloy, to 63% in the 2198–0.05Zr–0.3Mn alloy and 100% in the 2198–0.4Mn alloy, which was fully recrystallized. However, this sequence did not agree with the order of increasing net Zener dispersoid pinning ratio, which was highest for the 2198–0.1Zr–0.3Mn

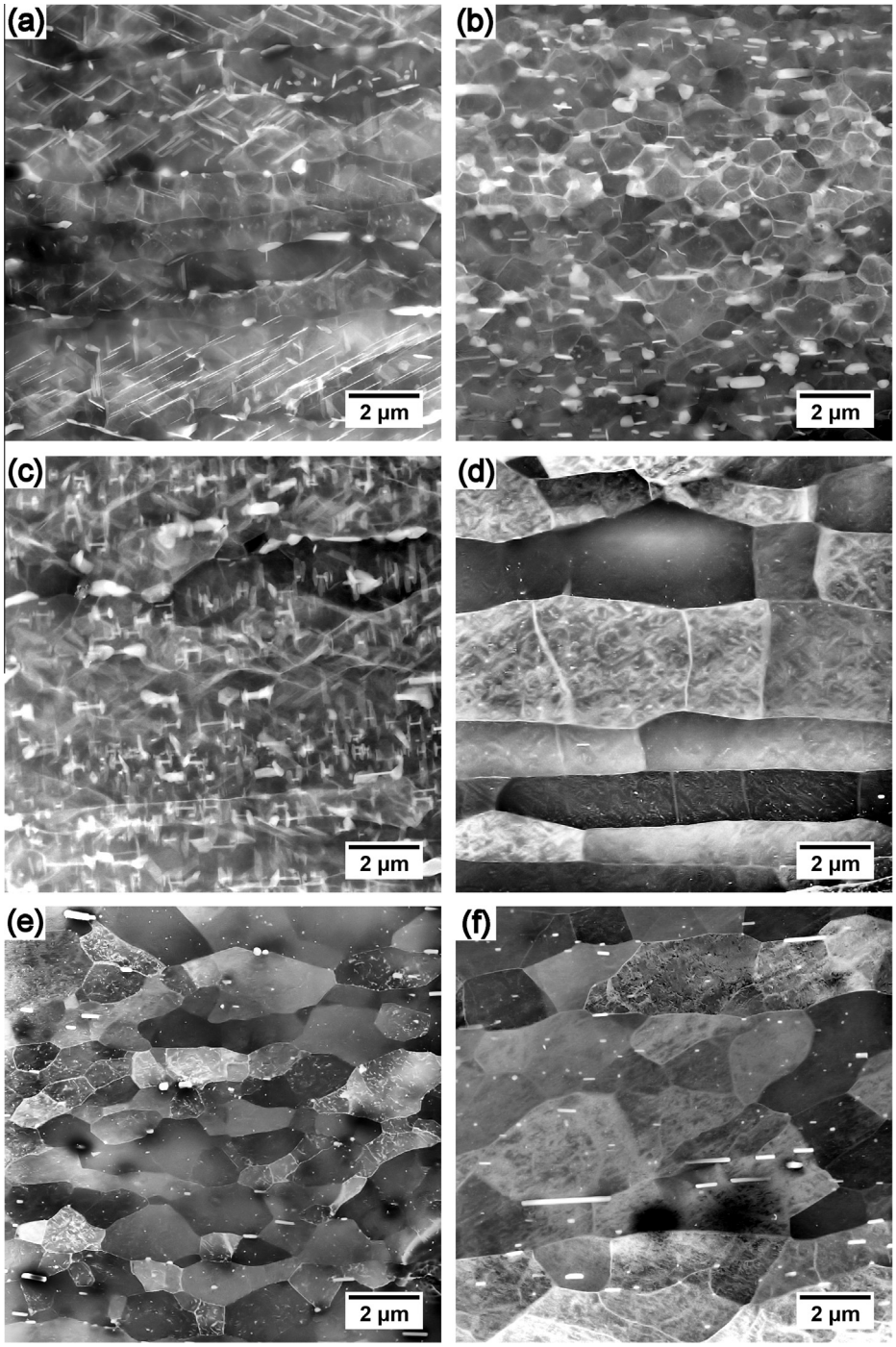

Fig. 2. Subgrain morphologies seen for the alloy variants, in RD–ND sections at the sheet centre, for the alloy variants in F and T351 tempers: (a) 2198–0.1Zr-D (F), (b) 2198–0.1Zr–0.3Mn (F), (c) 2198–0.4Mn (F), (d) 2198–0.1Zr (T351), (e) 2198–0.1Zr–0.3Mn (T351) and (f) 2198–0.4Mn (T351).

alloy (Table 2). Indeed, even the 2198–0.1Zr-D material, which contained a coarser Al_3Zr dispersoid distribution than the standard 2198–0.1Zr material, exhibited a lower level of recrystallization than any of the Mn-containing alloys. An interesting observation from these results was that when the same amount of Zr that was present in the standard 2198 alloy was used together with Mn in the 2198–0.1Zr–0.3Mn alloy, the recrystallized volume fraction increased from near zero to 14%, relative to when Zr was employed alone, despite the 2198–0.1Zr–0.3Mn alloy having the highest f_v/r ratio. As expected from the more recrystallized microstructures, the alloys with lower or no Zr content showed a large increase in HAGB ND spacing (Fig. 4b).

3.4. Recrystallization kinetics at 535 °C

To study their recrystallization kinetics, all the alloys were annealed within the solution treatment temperature range of the base material (~505–540 °C) [61] at 535 °C

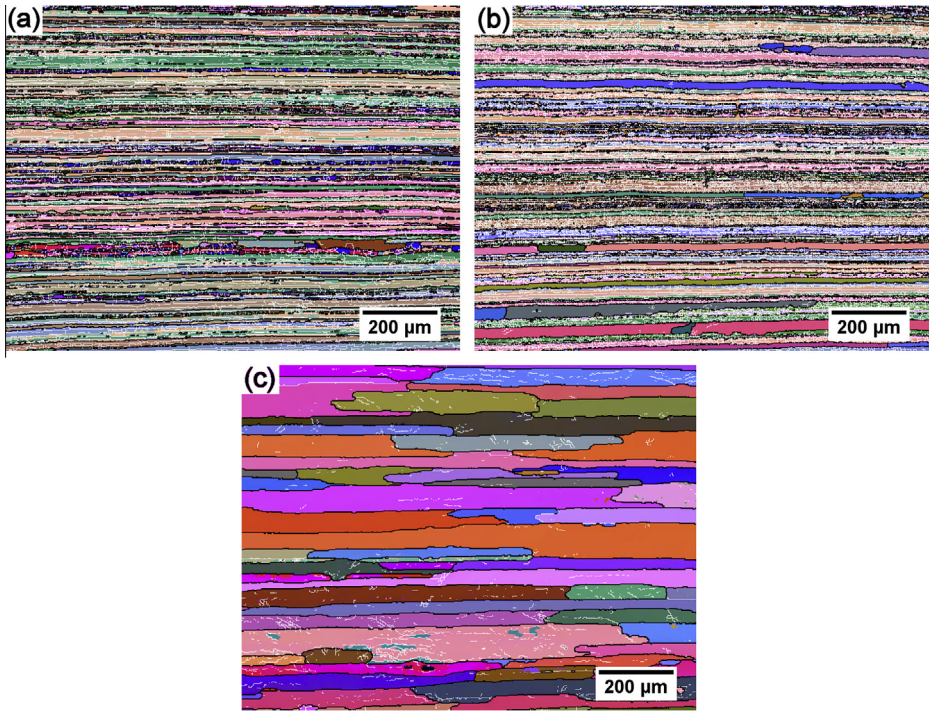

Fig. 3. Euler angle coloured EBSD maps from the sheet mid-plane after solution treatment (T351), comparing the levels of recrystallization seen in the alloys: (a) 2198–0.1Zr, (b) 2198–0.1Zr–0.3Mn and (c) 2198–0.4Mn.

for up to 144 h. The materials were heat treated from the as-hot rolled F temper (Fig. 5a), but due to the unavailability of the standard 2198–0.1Zr alloy in this condition, samples were also heat treated starting from the T351 condition (Fig. 5b). As can be seen from Fig. 5, when annealed from both starting conditions, the materials exhibited trends consistent with the recrystallized volume fractions seen in the as-received T351 microstructures. Isothermal annealing thus confirmed that alloys with a higher Zr and lower Mn level were more resistant to recrystallization. In the alloys annealed from the F temper, the alloy containing only Zr, 2198–0.1Zr-D, still exhibited the lowest levels of recrystallization. Even after 144 h heat treatment its recrystallized area did not exceed 15%, despite the "D" homogenizing treatment resulting in coarser Al_3Zr dispersoids, whereas the 2198–0.4Mn alloy fully recrystallized within 5 min at 535 °C. In comparison, the 2198–0.1Zr–0.3Mn alloy exhibited an intermediate behaviour: first recrystallizing rapidly to a level of ~17%, followed by stagnation with a subsequent slow increase in the level of recrystallization to ~35% after 72 h, and then showing a steeper rise to 55% after 144 h. The 2198–0.05Zr–0.3Mn alloy with a lower Zr content recrystallized much more rapidly, reaching complete recrystallization after 5 h. When starting from the T351 temper, the 2198–0.1Zr alloy (which in this condition had received the same homogenization treatment as the other materials) was again more resistant to recrystallization than all the other alloys, exhibiting only a level of ~7% recrystallization after prolonged annealing (144 h).

3.5. Recrystallization mechanisms

To better understand the dominant recrystallization mechanisms operating in the alloy variants, as a function of their Zr and Mn content, samples were selected for further analysis from each alloy at annealing times corresponding to a low volume fraction of recrystallization (<10%).

3.5.1. Recrystallization in the baseline alloy containing only Zr

Fig. 6 shows some examples from the few recrystallized regions found in the baseline 2198–0.1Zr alloy in the T351 condition and also after a short 1 h annealing treatment at 535 °C. In Fig. 6a, a band of grains, or a very elongated interconnected recrystallized grain, can be seen growing with a near-S orientation that originated from the unrecrystallized microstructure below it in the image. This S band appears to have consumed a neighbouring band of Brass orientation in the deformation structure (shown above in Fig. 6a) but still contains LAGBs in its lower section. Elongated grains which appeared to be recrystallizing in a similar manner, but with Cube, P, Copper and random orientations (white), are shown in Fig. 6b after annealing for 1 h at 535 °C from the F temper. These grains also still contained areas where LAGBs were present, which probably correspond to the region delineated by the original position of a HAGB before it migrated. This recrystallization mechanism is thus indicative of SIBM [32–34,40–44] and

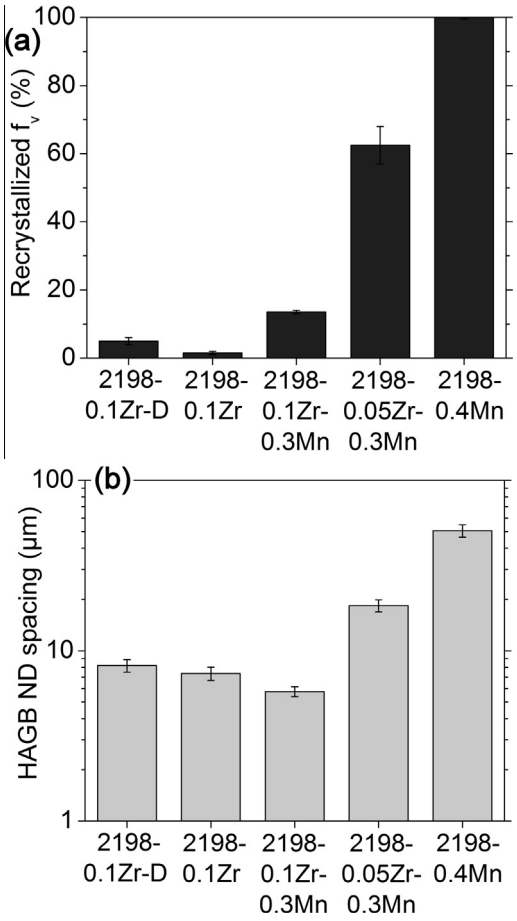

Fig. 4. (a) Area fraction of recrystallization (RD–ND plane), and (b) HAGB spacing in ND, for all the alloy variants in the T351 temper, obtained from EBSD data.

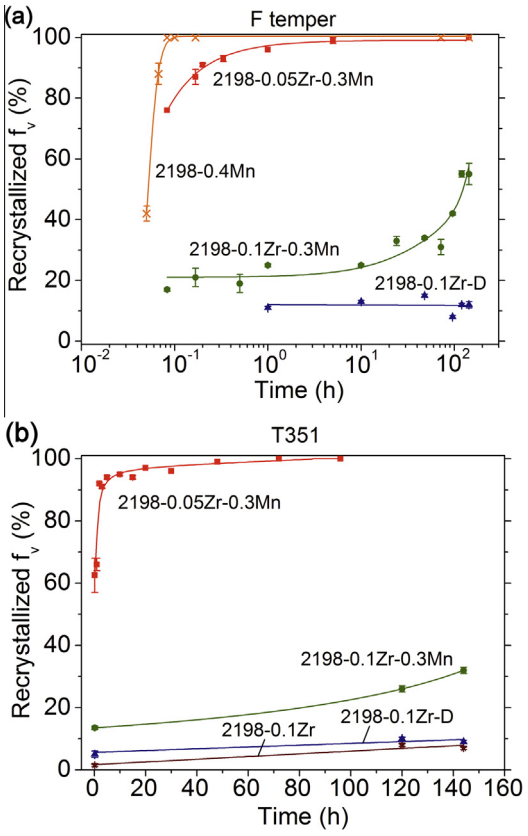

Fig. 5. Fractions of recrystallization plotted against annealing time measured from EBSD maps (RD–ND plane, mid-thickness) for all the alloy variants when starting in (a) the F temper, and (b) the T351 condition.

arrows showing the probable direction of boundary migration are indicated in Fig. 6b.

Although SIBM was the most frequent recrystallization mode observed in the 2198–0.1Zr material, it was not the sole process. In several instances recrystallized grains were found that contained aligned etch pits formed from large constituent particles that fell out during sample preparation by electropolishing (e.g. Fig. 6c and d). These particles were aligned with the RD so that it is likely they were originally situated on a grain boundary in the rolled microstructure. They also tended to be found in recrystallized grains with random orientations. Hence, it is quite likely that such grains were nucleated by PSN [32–39].

3.5.2. Recrystallization in the alloy containing only Mn

The 2198–0.4Mn alloy fully recrystallized very rapidly at 535 °C, by ~40% within 3 min, and examples of recrystallized grains for this condition are shown in Fig. 7a. In this alloy the role of the constituent particles was much more evident. In the EBSD band contrast map in Fig. 7b, several recrystallized grains can be seen that are associated with fairly large particles of the order of a few microns in size. Within the EBSD map shown, 8 out of the 16 recrystallized grains either contained (or were in contact with) one or more coarse particle in the section plane. Bearing in mind that grains are more likely to contain particles not intersecting the plane of view, this strong association is indicative of PSN dominating the recrystallization behaviour in this alloy. SIBM was also found to operate in the 2198–0.4Mn alloy, albeit at a much lower frequency. Evidence of this alternative mechanism is apparent in the EBSD map in Fig. 7c, where a high aspect ratio grain (appearing in white as randomly oriented) can be seen to have grown into a region previously occupied by either a Copper band or an S band. On the right edge of the grain a region of retained subgrain boundaries can again be observed, similar to that noted above in the case of the 2198–0.1Zr alloy.

3.5.3. Recrystallization in the 2198–0.1Zr–0.3Mn alloy

The most interesting case was that of the 2198–0.1Zr–0.3Mn alloy because it contained both dispersoid families. In Fig. 5a this was shown to lead to a complex shape in the recrystallization curve, since a low fraction of recrystallized grains started appearing after only 3 min annealing and then recrystallization stagnated for ~72 h at ~20%, before accelerating again. Early recrystallization in the 2198–0.1Zr–0.3Mn alloy was found to develop mainly elongated grains with random orientations, as can be seen from

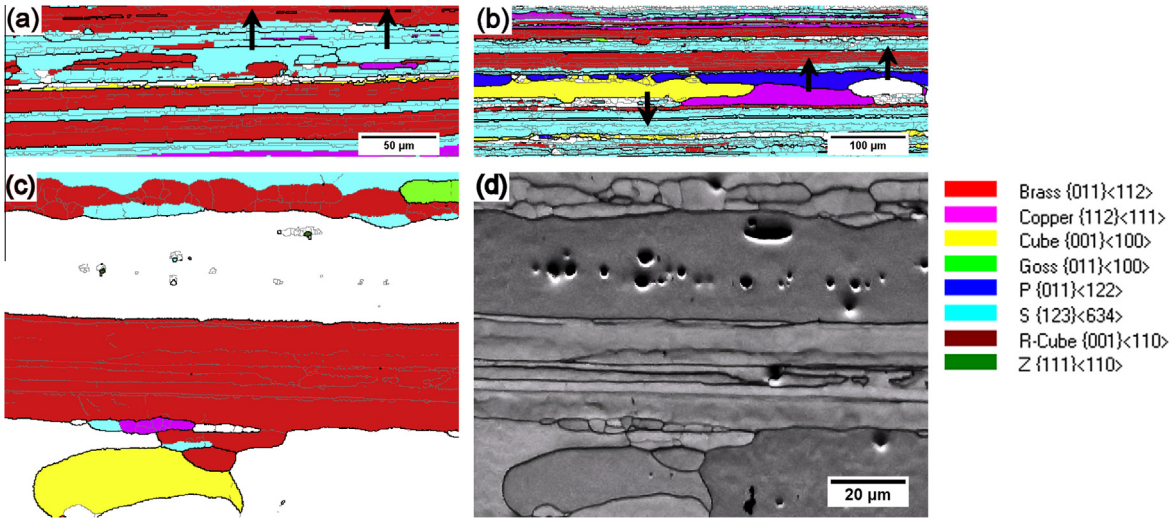

Fig. 6. Examples of the early stages of recrystallization in the 2198–0.1Zr-D alloy: (a) EBSD texture component map showing an S-oriented band growing into a Brass-oriented region (T351), (b) similarly for grains with Cube, P and Copper orientations (T351), and (c) a grain of random orientation containing coarse particles shown by etch pits in a band contrast map in (d), all following a solution treatment of 1 h at 535 °C from T351.

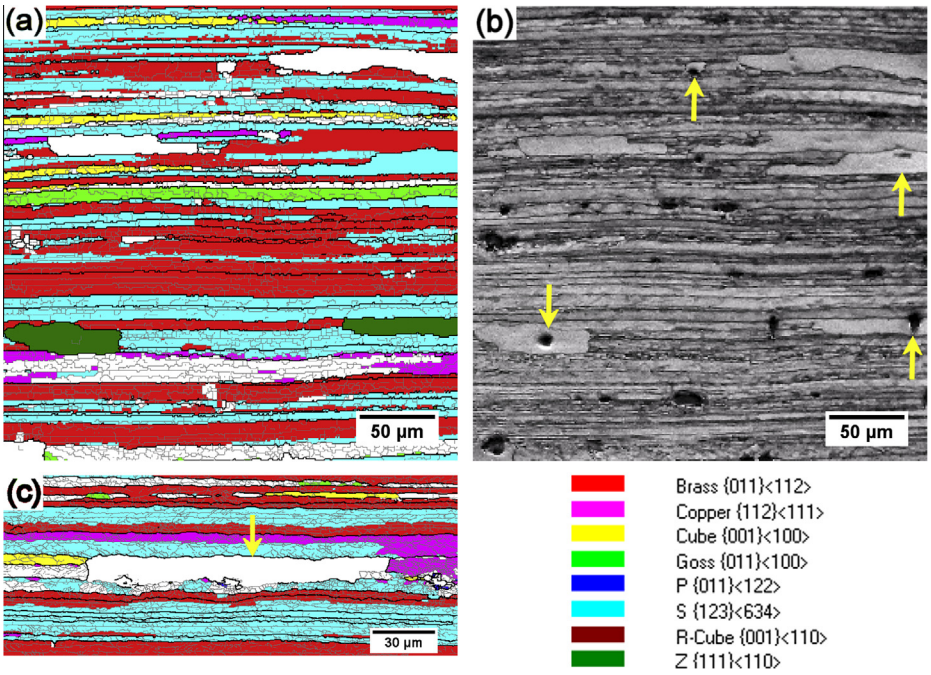

Fig. 7. The early stages of recrystallization in the 2198–0.4Mn alloy: (a) EBSD texture component map showing recrystallized grains of various orientations (annealed for 3 min at 535 °C); (b) EBSD band contrast map of the same area illustrating the association of large constituent particles with recrystallized grains; and (c) EBSD texture map showing a less frequent example of what is probably SIBM in the same alloy (annealed for 90 s at 535 °C).

Fig. 8a. SIBM was also seen to take place in this alloy, but this did not generally lead to a random grain orientation. Fig. 8b presents an example of a grain in the process of growing by SIBM by forming a bulging boundary of S orientation, similar to the surrounding recovered substructure. This mechanism became more widespread only after longer annealing times.

The early recrystallization in this alloy was found to occur primarily within bands of Mn dispersoids, as shown in Fig. 9a after 4 min at 535 °C. In the same TEM montage image, two recrystallized grains are visible and each is associated with a Mn dispersoid band. In the areas between these bands, few $Al_{20}Cu_2Mn_3$ particles were present and a high density of Al_3Zr dispersoids was found. This correlation was observed regardless of the nucleation mechanism responsible for the recrystallized grain. However, Mn dispersoid-rich bands that were not associated with recrystallized grains were also seen at this stage. Fig. 9b also presents an example of a large constituent particle situated right on the grain boundary of a recrystallized grain, which the adjacent recrystallized grain probably originated from.

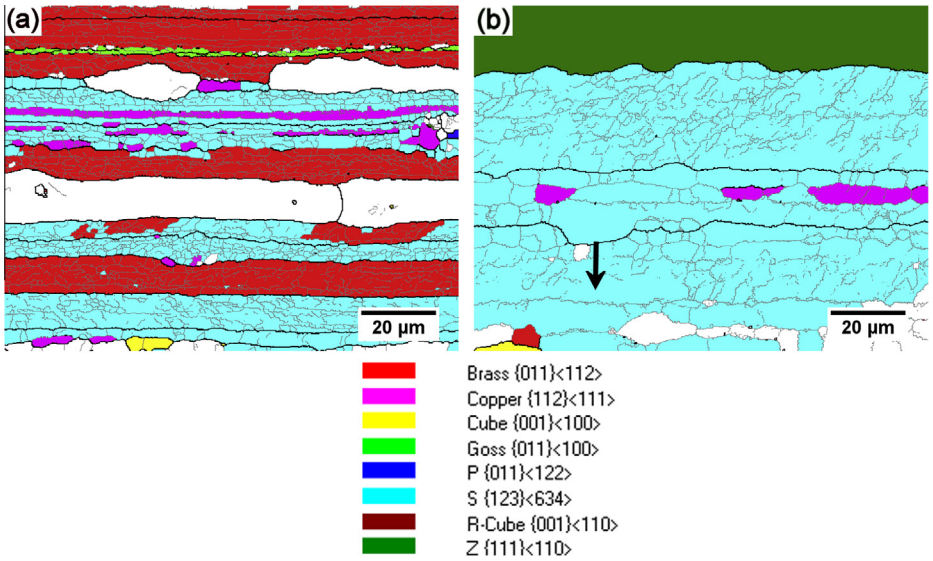

Fig. 8. The early stages of recrystallization in the 2198–0.1Zr–0.3Mn alloy: (a) EBSD texture component map showing high aspect ratio recrystallized grains of predominantly random orientation (T351); and (b) an example of a bulging SIBM nucleus in the same alloy (24 h at 535 °C).

3.6. Texture development

To see if the different dispersoid densities influenced the texture, EBSD analysis was performed on the F temper (as-hot rolled) materials and at progressive stages during annealing. {1 1 1} pole figures for the T351 starting condition are shown in Fig. 10, which indicate that texture was strongly affected by the level of recrystallization in each material. The texture was strongest in the nearly unrecrystallized 2198–0.1Zr alloy, with a maximum value of 19.8 × random, but became very weak and ill-defined in the fully recrystallized 2198–0.4Mn material.

The EBSD data were also differentiated into the unrecrystallized and recrystallized areas and the volume fractions of the major texture components were then plotted against annealing time for the four alloy variants. In Fig. 11 it is apparent that in the F temper the deformation textures in all cases were dominated by the S and Brass components, while all other orientations on the normal β rolling fibre had a low intensity. In the 2198–0.1Zr alloy there was little change with annealing time because the material remained largely unrecrystallized, even after 144 h at 535 °C (note that for this alloy the recrystallized texture data has been omitted because it was statistically poor owing to the very low level of recrystallization). In the 2198–0.4Mn alloy, both the S and Brass components can be seen to decrease simultaneously on annealing to be replaced by a largely random texture as the material recrystallized. In contrast, the 2198–0.1Zr–0.3Mn alloy initially showed a gradual reduction in the S and Brass fractions, corresponding to the stagnation behaviour described above. Fig. 11c shows that the 2198–0.4Mn alloy probably initially followed a similar trend, but did not stagnate in its level of recrystallization, and the Brass level was already higher in this alloy in the starting condition. In Fig. 11, it can be further noted that the recrystallization textures in all the Mn-containing alloys were dominated by random components.

4. Discussion

The recrystallization studies performed in this work, during extended annealing at solution treatment temperatures, have confirmed a previous observation that the addition of Mn increases the level of recrystallization seen in a Zr-containing AA2198 alloy when processed to hot-rolled sheet [14,23], which is the opposite effect to that originally intended. In a previous publication, this behaviour was shown to be caused by subtle interactions that take place when Mn is used jointly with Zr as a dispersoid former in Al–Cu–Li alloys, which affects the density and spatial distribution of Al_3Zr dispersoids present in the rolled material. It was previously shown that the addition of 0.3 wt.% Mn to the 2198–0.1Zr baseline alloy caused a small average reduction in the number density and an increase in the size of the Al_3Zr dispersoids, which led to a modest overall reduction in the average Zener pinning pressure (Table 2). This behaviour was found to be caused by a slight reduction in the Zr supersaturation available for precipitation of Al_3Zr dispersoids during homogenization, and occurred because a low concentration of Zr became dissolved in Mn-bearing phases. However, model predictions showed that this small reduction in Zr supersaturation had a disproportionate effect on the Al_3Zr density near grain boundaries, where there was already a low Zr supersaturation because of inverse segregation during casting, and was sufficient to double the width of Al_3Zr dispersoid-free bands present in a rolled sheet. This increase in Al_3Zr dispersoid-free band width was particularly significant because, at these relatively high rolling reductions, the precipitate-free band width in the original Mn-free AA2198 baseline alloy was of a similar scale to that of the substructure. The doubling

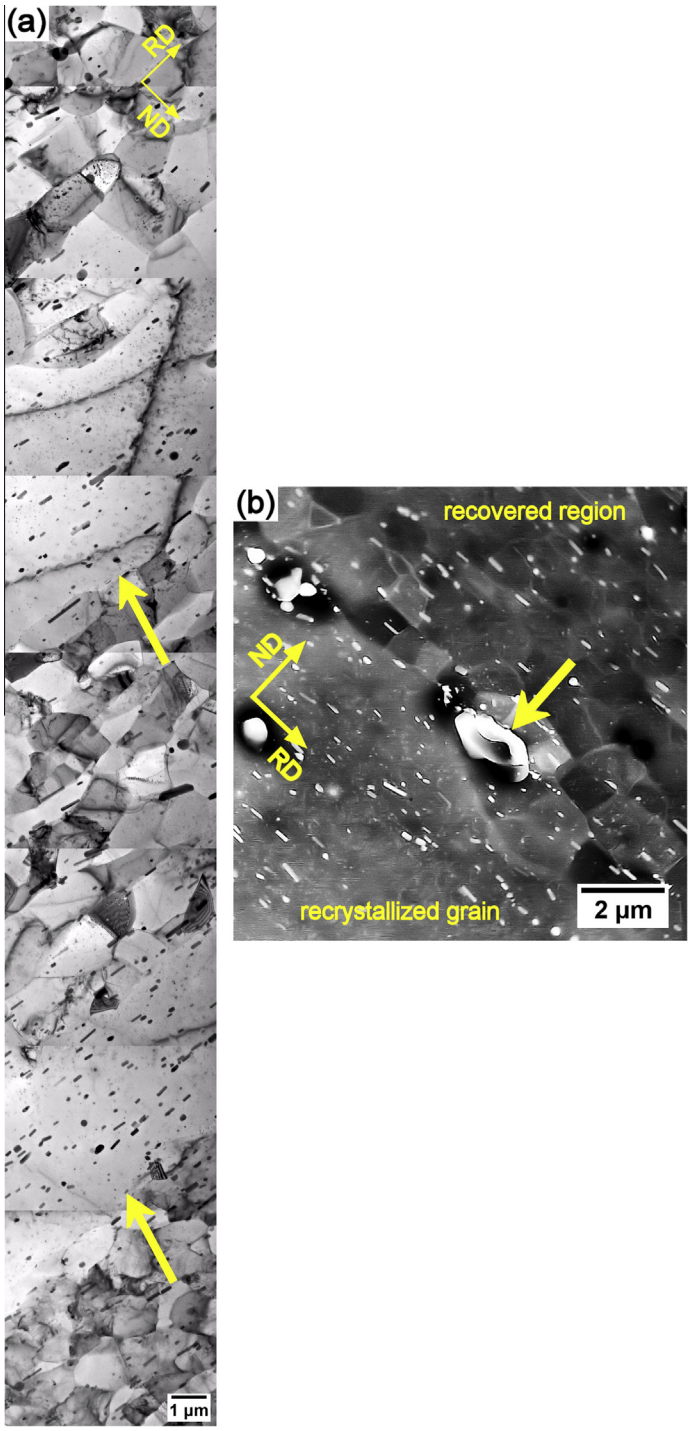

Fig. 9. TEM images from the 2198–0.1Zr–0.3Mn alloy (annealed for 4 min at 535 °C) showing: (a) recrystallization within Mn dispersoid-rich bands; and (b) a possible PSN nucleus within the deformation zone imaged via HAADF-STEM.

of the Al_3Zr dispersoid-free band width that resulted from adding Mn, while retaining the same Zr level, thus increased the fraction of recrystallization from close to zero to 14%, as has been demonstrated again above in more detail (Figs. 4 and 5).

However, the argument in this earlier paper was largely based on noting that the Mn dispersoids were ineffective in preventing recrystallization in the baseline material, when rolled to sheet, and the discussion focused on the effect of Mn on the precipitation behaviour of the Al_3Zr dispersoids and their spatial distribution across the bands they formed. This paper thus left some unanswered questions, which will be discussed here in the light of the new data presented above. In particular, if the Zener pinning ratio data is considered in Table 2 it is surprising that the Mn dispersoids are so ineffective relative to the Al_3Zr dispersoids they

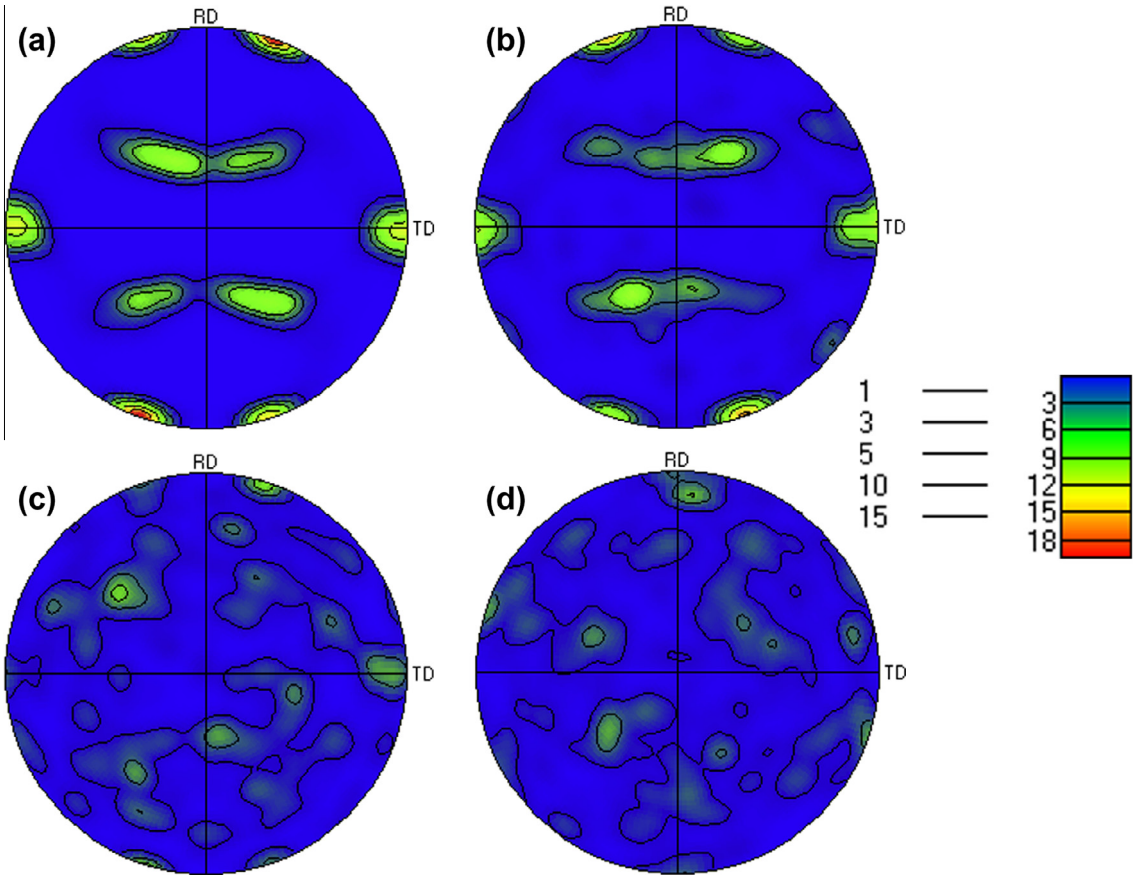

Fig. 10. {1 1 1} pole figures showing the textures of the AA2198 alloy variants in the T351 temper: (a) 2198–0.1Zr ($f(g)_{max} = 19.8$), (b) 2198–0.1Zr–0.3Mn ($f(g)_{max} = 15.7$), (c) 2198–0.05Zr–0.3Mn ($f(g)_{max} = 6.1$) and (d) 2198–0.4Mn ($f(g)_{max} = 5.1$).

replace. For example, the average f_v/r ratio for the $Al_{20}Cu_2Mn_3$ phase in the 2198–0.1Zr–0.3Mn alloy ($f_v/r = 0.07$) is comparable to that for the Al_3Zr dispersoids in the 2198–0.1Zr baseline material ($f_v/r = 0.09$). In fact, in the 2198–0.4Mn alloy f_v/r is actually 30% higher than for the Al_3Zr dispersoids ($f_v/r = 0.12$). In addition, when the net effect of both dispersoid families is considered, the total average Zener pinning ratio is substantially higher in the 2198–0.1Zr–0.3Mn alloy ($f_v/r = 0.15$) that recrystallized, compared to the 2198–0.1Zr material ($f_v/r = 0.09$) which did not. Furthermore, the Mn dispersoids are not homogeneously distributed, due to positive partitioning of Mn during solidification, and tend to be concentrated near the grain boundaries present in the original cast structure that are elongated in the rolling process. Such boundaries are often found to be sites of recrystallization because they are frequently associated with primary particles inherited from the cast structure [62].

4.1. Effect of Mn addition on stored energy

It is apparent from Figs. 1 and 2 that the two different dispersoid types had a notable effect on their comparative stored energy prior to annealing. The 2198–0.1Zr–0.3Mn alloy had the smallest subgrain size and the estimates presented suggest that after hot rolling the stored energy for this alloy was ~30% greater than that of the 2198–0.1Zr-D material. Classical work by Ashby [63] has shown that small non-shearable particles generate additional "geometrically necessary" dislocations the density of which, ρ, has a similar dependence on volume fraction and particle size as P_Z (Eq. (1)):

$$\rho = 3\frac{f_v}{r}\frac{\varepsilon_s}{b}, \tag{3}$$

where ε_s is the shear strain and b is the Burgers vector. Thus, the rate at which additional dislocations are formed by the dispersoid particles as a function of strain will increase in proportion to the same f_v/r ratio as their pinning pressure. Larger particles are also more effective at multiplying dislocation loops during deformation by promoting cross-slip [64]. The addition of Mn to the 2198–0.1Zr alloy will hence increase the rate of dislocation generation. However, the dislocation density will be limited by recovery and the associated formation of cellular structures during hot working. The additional Mn in solution, which after precipitation of the dispersoids during homogenization would be ~0.18 wt.% [23], could, therefore, be important in this context in inhibiting recovery. However, according to Westengen et al. [65], the effect of Mn solute on inhibiting recovery and recrystallization depends on the alloy system's composition, due to interactions with

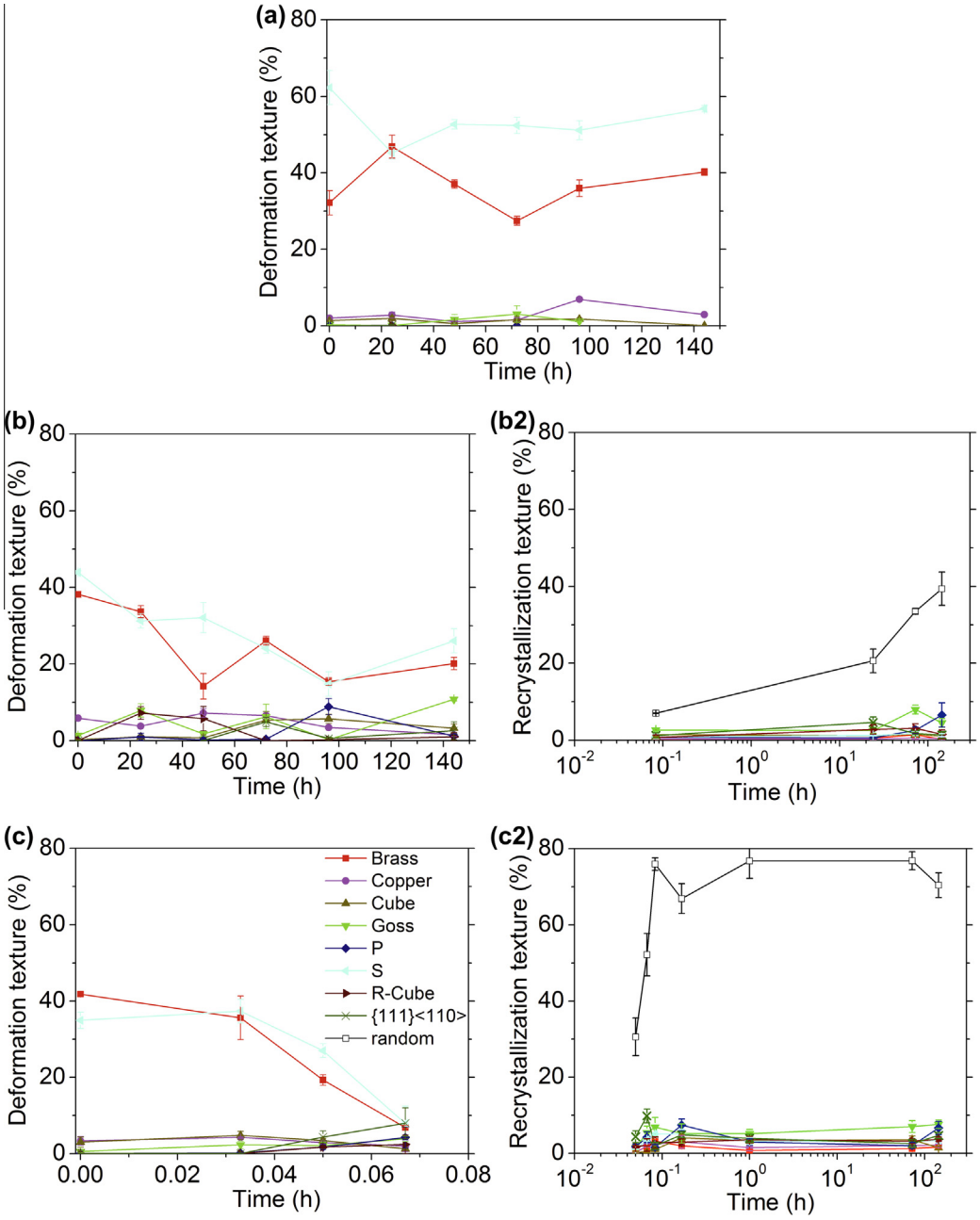

Fig. 11. Area fractions of the main texture components measured in the deformed and recrystallized regions of the (a) 2198–0.1Zr, (b) 2198–0.1Zr–0.3Mn and (c) 2198–0.4Mn alloys as a function of annealing time at 535 °C.

the rest of the alloying elements, and is significantly more pronounced in dilute alloys than commercial alloys.

4.2. Effect of dispersoids on boundary mobility

There have been numerous attempts over the years to modify the original Zener relationship given in Eq. (1) to take into account the effect of different types of particle morphology and coherency [60,66–69]. From this work it is clear that coherent particles that lose their coherency on passage of a grain boundary are more effective than incoherent particles in pinning a boundary by a maximum factor of two [66]. This would suggest that, relative to the effectiveness of the $Al_{20}Cu_2Mn_3$ particles, the f_v/r ratio for the Al_3Zr dispersoids should be doubled. Furthermore, while both sets of dispersoids are banded in the rolled sheet, the Al_3Zr particles are spherical, whereas the $Al_{20}Cu_2Mn_3$ are lath-shaped and are aligned in the rolling plane. This means they will exert a different pining pressure in different directions as the surface area of a grain boundary that interacts with the particle will depend on the particle orientation. This effect has been modelled for the case of ellipsoidal particles with eccentricity ε by Nes et al. [66] who obtained the relationships:

$$\frac{P_z^{\varepsilon}}{P_z^{s}} = \frac{2}{(1+\varepsilon)\varepsilon^{1/3}} \quad (4)$$

$$\frac{P_z^{\varepsilon}}{P_z^{s}} = \frac{1+2.14\varepsilon}{\pi\varepsilon^{1/2}} \quad (5)$$

that describe the drag force, P_z^{ε}, for particles interacting end-on (Eq. (4)) and edge-on (Eq. (5)) with a boundary, relative to that for spherical particles, P_z^{s}, with the same volume fraction. Using the data in Table 2 it can be estimated that, from their geometry alone, the elongated $Al_{20}Cu_2Mn_3$ particles will be nearly half as effective at providing a boundary pinning pressure in RD as the measured value of f_v/r would imply, which was determined using their equivalent circular diameter. However, in ND they would be expected to be nearly twice as potent. Thus, taking into account their lack of coherency and their alignment, for the same f_v/r ratio, the $Al_{20}Cu_2Mn$ dispersoids will be less effective at preventing boundary mobility in RD than the Al_3Zr particles by a factor of about four. Furthermore, although the larger cross-section of the Mn particles in ND offers a higher pinning force, it has been suggested that a "ledge propagation" mechanism [67,70] can be responsible for the easier bypassing of a lath-shaped particle by a boundary when migrating perpendicular to its long edge, as the boundary can still move laterally along its major axis. A probable example of this mechanism in operation is shown in Fig. 12, where a boundary pinned by the wide edge of a lath-shaped $Al_{20}Cu_2Mn_3$ dispersoid is seen to be moving sideways at the point of contact to slip off the particle's end parallel to its long axis.

For the extended annealing treatments investigated it is apparent that the dispersoid particles will coarsen with time and this will slowly reduce their net pinning pressure. However, in the case of the 2198–0.1Zr alloy significant recrystallization did not occur even after annealing for 144 h. Equally, the mechanism of recrystallization did not change and was still dominated by broad-front SIBM. In comparison, in the 2198–0.4Mn alloy recrystallization occurred rapidly by PSN as the dispersoid particle density was already too low from the start of annealing to prevent recrystallization, even without significant coarsening. The intermediate case of the 2198–0.1Zr–0.3Mn alloy with joint Zr and Mn additions showed rapid initiation of recrystallization and then stagnation. In this alloy recrystallization initiated early in regions where there was a lower Al_3Zr dispersoid density and then developed very slowly at a rate that would, therefore, be expected to be strongly affected by coarsening of the Al_3Zr dispersoids.

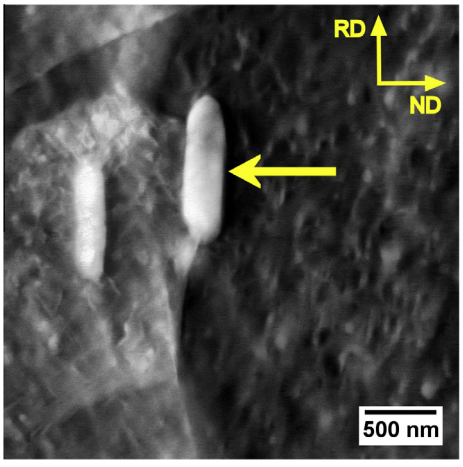

Fig. 12. Interaction between an elongated Mn dispersoid and a migrating grain boundary, illustrating the "ledge propagation" mechanism of GB motion.

The coarsening kinetics of the Zr and Mn dispersoids have been presented in a previous publication (Fig. 10 in Ref. [23]) which showed that the Al_3Zr dispersoids increased in size from around ~20 nm to ~55 nm after 144 h annealing. If the particles retain their coherency, this would reduce the average pining pressure by a similar factor of ~2.5. The critical diameter for coherency loss of the Al_3Zr phase was calculated to be ~70 nm. Thus, although there is a particle size distribution in the microstructure, the majority of the Al_3Zr dispersoids would be expected to remain coherent even at the longest annealing time of 144 h and the factor of 2.5 seems reasonable. When recrystallization is controlled by the slow rate of coarsening of pinning particles the stored energy will reduce simultaneously with the reduction in pinning pressure, in a process known as "extended recovery", and this can be an important factor in the stagnation of recrystallization, as was observed for the 2198–0.1Zr–0.3Mn alloy [32].

It was also found previously (Fig. 10 in Ref. [23]) that the Mn dispersoids increased in equivalent diameter from ~75 nm to ~125 nm in the 2198–0.1Zr–0.3Mn alloy on annealing for 144 h, but did not spheroidize. In contrast, they coarsened more along their long and less along their short axis, increasing their aspect ratio. For the same equivalent particle diameter this effect would cause a slight increase in the overall pinning pressure in ND according to Eq. (5), but it could equally be argued that this would be counteracted by promoting the ledge propagation mechanism of boundary migration which was analyzed earlier. In any event, the Mn dispersoids were not able to prevent recrystallization on their own even prior to any coarsening occurring, and thus coarsening of the Mn dispersoids would not be expected to change the recrystallization mechanisms in any of the Mn-containing alloys.

4.3. Recrystallization mechanisms

From the above discussion it is apparent that the $Al_{20}Cu_2Mn_3$ dispersoids are less effective than Al_3Zr particles in preventing recrystallization in sheet Al–Cu–Li alloys that have undergone a large rolling reduction. In particular, the boundary pinning pressure they provide has been estimated to be about four times less than that of the Al_3Zr particles, while at the same time they increase the stored energy in the hot-rolled material. In the materials studied, the balance between driving force and pinning pressure,

therefore, favoured recrystallization in the 2198–0.4Mn alloy variant. Similarly, in the case of joint Zr and Mn additions recrystallization was possible within the $Al_{20}Cu_2Mn_3$ dispersoid-rich bands because the width of the Al_3Zr-free region was widened by the addition of Mn, due to the Mn–Zr interaction previously discussed [23].

In addition, it is also apparent that the inclusion of Mn in the 2198 alloy at the expense of Zr changed the dominant recrystallization mechanism and texture development during heat treatment. The main mechanism of recrystallization seen in the 2198–0.1Zr alloy, which exhibited a very low level of recrystallization even after extensive heat treatment, was identified to be SIBM. Because the growing grain develops by the migration of a pre-existing grain boundary, SIBM has the characteristic feature that it will normally retain a main rolling component and can leave behind a region that still contains LAGBs or even drag out LAGBs behind the migrating boundary [32–34,40–44]. This is evident in several grains in Fig. 6. When there are high pinning pressures, as provided by the Al_3Zr dispersoid distribution, this mechanism has also been previously reported to tend to operate across a broad front, leading to the formation of grains highly elongated along RD [45,46]. Again, examples of this behaviour are shown in Fig. 6a and b. The initiation of broad-front SIBM will also be favoured by the elongated grain structure and the low-density Al_3Zr dispersoid bands present in the starting microstructure.

In contrast, as the Mn content was increased and the Al_3Zr dispersoid density reduced, PSN became more prevalent in the 2198–0.4Mn alloy until it dominated the recrystallization process. In aluminium alloys PSN normally originates from highly misorientated subgrains within the deformation zones surrounding constituent particles, but this can be inhibited by a high density of fine dispersoids in the matrix which increases the critical nucleus size beyond that of the primary particles' deformation zones [6,32]. PSN was observed in the 2198–0.1Zr–0.3Mn alloy to occur at short annealing times within Mn-rich (and Al_3Zr-free) bands. However, this still gave rise to elongated grains due to the banding of the Al_3Zr dispersoids, which caused recrystallization to stagnate once it had expanded to cover the regions of low Al_3Zr density in the rolled material (Fig. 6). Such grains can also be distinguished in Fig. 8 from their random orientations. SIBM was also observed in the alloys with joint Zr and Mn additions (Fig. 8b), but was not as prevalent as PSN. A further factor that would favour PSN on the addition of Mn is through an increase in the number of potential PSN sites in the material. For example, it is known that Mn can be combined with Fe and Cu within constituent particles which can increase their volume fraction [24,71,72].

Finally, the loss of the more effective Al_3Zr dispersoids resulted in a fully recrystallized microstructure in the 2198–0.4Mn alloy and a lower aspect ratio grain structure. The high association of recrystallized grains seen in the early stages of recrystallization with constituent particles, and their random orientations, suggests that recrystallization in this material occurred almost exclusively by PSN.

4.4. Effect of dispersoid content on texture

The level of recrystallization and the dominant recrystallization mechanism can have a major role in the preferential consumption or growth of deformation texture components during solution treatment [73]. In common with other Al–Cu–Li alloys [74–76], the main deformation texture components seen after hot rolling in all the AA2198 alloy variants were S and Brass (Fig. 11). However, in the starting hot deformation textures a significant difference could be observed (Fig. 11), in that in the as-hot rolled textures in the 2198–0.1Zr baseline alloy the S component was stronger than Brass, but in the Zr-free Mn-containing alloy the fraction of Brass was marginally higher than S. This trend could potentially be related to the fact that the Mn-containing alloys were more prone to recrystallization and consequently they may have already partially recrystallized between hot-rolling passes, which could change the balance between Brass and S because the latter component develops more strongly at large rolling strains [32,77].

During extended solution treatment in the Mn-containing alloys PSN was found to be the dominant recrystallization mechanism (Figs. 7 and 8). In PSN it is well known that the nucleus is formed in the deformation zone around a particle that contains a large spread of local misorientations, and therefore the recrystallization front will migrate and consume the surrounding substructure irrespective of its particular β-fibre orientation [32,33]. Thus, on annealing the Mn-containing alloy variants, both the S and Brass components would be expected to be consumed to a similar extent and replaced by a more random texture. This can be verified by the observation that the volume fraction of S and Brass components reduced at a similar rate, as the level of recrystallization increased, in all the Mn-containing alloys during extended annealing (Fig. 11).

In contrast, in the baseline alloy containing only Zr, broad-front SIBM was found to be the main mechanism of recrystallization. In SIBM grain boundary migration occurs due to a differential in stored energy across a HAGB segment separating grains that have defined orientations within the deformation texture; new orientations are thus not expected to be generated by this process [32]. However, in SIBM if specific components have a systematic growth advantage they can potentially increase in intensity and others can reduce. Hence, when SIBM dominates recrystallization this leads to the retention of the original deformation texture in the annealed microstructure. This behaviour can be seen in Fig. 11a where in the AA2198–0.1Zr alloy the S and Brass component volume fractions remained fairly constant at all annealing times. In this alloy the ratio of S to Brass also did not change significantly on annealing, suggesting that there was no particular preference for SIBM to initiate within a particular texture component. However, given the low volume

fraction of recrystallization, it would be difficult to detect a subtle preference for one particular texture component to increase in volume fraction within the experimental scatter without performing more repeated texture measurements, which was not possible in the current study.

5. Conclusions

In this work the effect of Mn and Zr dispersoid-forming additions on the recrystallization behaviour of an Al–Cu–Li alloy has been investigated, after hot rolling to 6 mm gauge sheet. It has been found that recrystallization resistance diminishes as Zr is progressively replaced with Mn. More importantly it has been confirmed that if Zr is maintained at a constant level and Mn is added to the standard 2198 alloy as a second dispersoid-forming element, this also results in a reduction in recrystallization resistance, despite the fact that the opposite microsegregation patterns of these two elements give a more complete coverage of dispersoids in a rolled product.

A reduction in effectiveness of the Al_3Zr dispersoids in inhibiting recrystallization on the addition of Mn has itself been reported previously by the present authors and results from an increase in the Al_3Zr dispersoid-free band width in hot-rolled Al–Cu–Li products. Here, it has been shown that the above observations can be explained largely by the high density of $Al_{20}Cu_2Mn_3$ dispersoids formed in the Al_3Zr dispersoid-free bands still not having adequate pinning pressure to compensate for the reduction in effectiveness of the Al_3Zr dispersoids. The lower potency of Mn relative to Zr in inhibiting recrystallization has been attributed to the poorer coherency and higher aspect ratio of the $Al_{20}Cu_2Mn_3$ dispersoids, which lowers their Zener pinning pressure by a factor of four relative to that of the Al_3Zr particles, when compared on the basis of the same volume fraction/equivalent spherical diameter ratio. In addition, it has been shown that the presence of coarser $Al_{20}Cu_2Mn_3$ dispersoids increased the stored energy prior to recrystallization by increasing the rate of generation of geometrically necessary dislocations during hot working and reducing the subgrain size prior to solution treatment.

The dominant recrystallization mechanism has been found to depend strongly on the dispersoid content in each alloy. The more effective dispersion of Al_3Zr particles in the 2198–0.1Zr alloy led to the dominance of broad-front SIBM, as a consequence of the high pinning pressure provided by the fine and coherent Al_3Zr dispersoids, whereas the lower pinning pressure and increase in nucleation site density on the addition of Mn favoured PSN. Recrystallization texture measurements verified this observation, since SIBM favoured the retention of deformation texture components on annealing, while PSN promoted the nucleation of more randomly orientated grains. Finally, the ratio of the main S and Brass deformation texture components observed in the hot-rolled microstructures was seen to reduce on increasing the alloy's Mn content relative to their Zr level. This effect has been attributed to partial recrystallization being more likely to occur between rolling passes in the Mn-containing alloys which weakens the S component.

Acknowledgements

The leading author would like to thank EPSRC for funding this research through LATEST2 (Light Alloys Towards Environmentally Sustainable Transport; EP/G022402/1). Both authors would like to thank Dr Christophe Sigli and Mr Bernard Bès of Constellium, Centre de Recherches de Voreppe, for financial support to the project and provision of materials.

References

[1] Warner T. Mater Sci Forum 2006;519–521:1271.
[2] Starke Jr EA, Lin FS. Metall Mater Trans A 1982;13:2259.
[3] Lavernia EJ, Srivatsan TS, Mohamed FA. J Mater Sci 1990;25:1137.
[4] Gokhale AM, Deshpande NU, Denzer DK. ICAA-4: 4th international conference on aluminium alloys. Atlanta, GA: 1994. p. 685.
[5] Jata KV, Vasudévan AK. Mater Sci Eng A 1998;241:104.
[6] Eschbach L, Uggowitzer PJ, Speidel MO. Mater Sci Eng A 1998;248:1.
[7] Wanhill RJH. Int J Fatigue 1994;16:3.
[8] Starke Jr EA, Staley JT. Prog Aerosp Sci 1996;32:131.
[9] Immarigeon JP, Holt RT, Koul AK, Zhao L, Wallace W, Beddoes JC. Mater Charact 1995;35:41.
[10] Lequeu P, Lassince P, Warner T. Adv Mater Processes 2007;165:41.
[11] Lequeu P. Adv Mater Processes 2008;166:47.
[12] Lequeu P, Smith K, Daniélou A. J Mater Eng Perform 2010;19:841.
[13] Jia Z, Hu G, Forbord B, Solberg JK. Mater Sci Eng A 2007;444:284.
[14] Tsivoulas D, Prangnell PB, Sigli C, Bès B. Adv Mater Res 2010;89–91:568.
[15] Morris PL, Ball MD. 1st Risø international symposium on metallurgy and materials science. Roskilde: 1980. p. 97.
[16] Cheong S, Weiland H. Mater Sci Forum 2007;558–559:153.
[17] Forbord B, Hallem H, Marthinsen K. ICAA-9: 9th international conference on aluminium alloys. Brisbane: 2004. p. 1179.
[18] Conserva M, Leoni M. Metall Trans A 1975;6:189.
[19] Kim YB, Chung YH, Cho KK, Shin MC. Scr Mater 1997;36:111.
[20] Chang J, Moon I, Choi C. Metall Mater Trans A 1998;29:1873.
[21] Feng X, Kumar AM, Hirth JP. Acta Metall Mater 1993;41:2755.
[22] Park DS, Nam SW. J Mater Sci 1995;30:1313.
[23] Tsivoulas D, Robson JD, Sigli C, Prangnell PB. Acta Mater 2012;60:5245.
[24] Tsivoulas D. PhD thesis, The University of Manchester, 2010.
[25] Murray J, Peruzzi A, Abriata JP. J Phase Equilib 1992;13:277.
[26] Vecchio KS, Williams DB. Acta Metall 1987;35:2959.
[27] Anselmino E, Miroux A, van der Zwaag S. Aluminium 2004;80:680.
[28] Zoeller TL, Sanders Jr TH. J Phys IV 2004;120:61.
[29] Dehmas M, Archambault P, Serriere M, Gautier E, Gandin C-A. Aluminium 2004;80:619.
[30] Mingard KP, Cantor B, Palmer IG, Hughes IR, Alexander PW, Willis TC, et al. Acta Mater 2000;48:2435.
[31] Nadella R, Eskin DG, Du Q, Katgerman L. Prog Mater Sci 2008;53:421.
[32] Humphreys FJ, Hatherly M. Recrystallization and related annealing phenomena. 2nd ed. Oxford: Elsevier; 2004.
[33] Humphreys FJ. Mater Sci Forum 2004;467–470:107.
[34] Gottstein G, Shvindlerman LS. Grain boundary migration in metals. Boca Raton, FL: CRC Press; 1999.
[35] Humphreys FJ. Acta Metall 1977;25:1323.
[36] Humphreys FJ. Acta Metall 1979;27:1801.
[37] Humphreys FJ. Scr Mater 2000;43:591.

[38] Ardakani MG, Humphreys FJ. Acta Metall Mater 1994;42:763.
[39] Ørsund R, Nes E. Scr Metall 1988;22:671.
[40] Beck PA, Sperry PR. J Appl Phys 1950;21:150.
[41] Bate P, Hutchinson B. Scr Mater 1997;36:195.
[42] Theyssier MC, Driver JH. Mater Sci Eng A 1999;272:73.
[43] Winning M. Scr Mater 2008;58:85.
[44] Kashihara K, Inoko F. Acta Mater 2001;49:3051.
[45] Higginson R, Bate P. Acta Mater 1999;47:1079.
[46] Somerday M, Humphreys FJ. Mater Sci Technol 2003;19:20.
[47] Hirsch JR. Recrystallization '90: international conference on recrystallization in metallic materials: conference proceedings. Wollongong: 1990. p. 759.
[48] Engler O, Lücke K. Scr Metall Mater 1992;27:1527.
[49] Engler O, Hirsch J, Lücke K. Acta Metall Mater 1995;43:121.
[50] Engler O. Metall Mater Trans A 1999;30:1517.
[51] Crumbach M, Goerdeler M, Gottstein G. Acta Mater 2006;54:3291.
[52] Liu J, Banovic SW, Biancaniello FS, Jiggets RD. Metall Mater Trans A 2005;36:869.
[53] Doherty RD. Prog Mater Sci 1997;42:39.
[54] Doherty RD, Hughes DA, Humphreys FJ, Jonas JJ, Jensen DJ, Kassner ME, et al. Mater Sci Eng A 1997;238:219.
[55] Vasudévan AK, Przystupa MA, Fricke Jr WG. Mater Sci Eng A 1996;208:172.
[56] Engler O, Hirsch J, Lücke K. Acta Metall 1989;37:2743.
[57] Lücke K, Engler O. Mater Sci Technol 1990;6:1113.
[58] ASTM E 562–02: standard test method for determining volume fraction by systematic manual point count.
[59] Humphreys FJ. VMAP suite of programmes for quantitative analysis of EBSD data. 2000.
[60] Manohar PA, Ferry M, Chandra T. ISIJ Int 1998;38:913.
[61] Materials science international team msit®. Al–Cu–Li (Aluminium–Copper–Lithium).. In: Effenberg G, Ilyenko S, editors. Non-ferrous metal systems. Part 2. Berlin: Springer Verlag; 2007. p. 1.
[62] Furrer P, Hausch G. Met Sci 1979;13:155.
[63] Ashby MF. Philos Mag 1966;14:1157.
[64] Hautefeuille L, Clavel M. Scr Metall 1988;22:1383.
[65] Westengen H, Auran L, Reiso O. Aluminium 1981;57:797.
[66] Nes E, Ryum N, Hunderi O. Acta Metall 1985;33:11.
[67] Hazzledine PM. Czech J Phys 1988;38:431.
[68] Ringer SP, Kuziak RP, Easterling KE. Mater Sci Technol 1991;7:193.
[69] Ringer SP, Li WB, Easterling KE. Acta Metall 1989;37:831.
[70] Chan HM, Humphreys FJ. Acta Metall 1984;32:235.
[71] Blanc C, Lavelle B, Mankowski G. Corros Sci 1997;39:495.
[72] Beauchesne J-T, Caillard D, Mompiou F, Ochin P, Quiquandon M, Gratias D. Z Kristallogr 2008;223:823.
[73] Humphreys FJ. Acta Mater 1997;45:4231.
[74] Shamrai VF, Grushko OE, Egiz IV, Borovskikh SN. Russ Metall (Metally) 2006;2006:176.
[75] Contrepois Q, Maurice C, Driver JH. Mater Sci Eng A 2010;527:7305.
[76] Cho A, Long Z, Lisagor B, Bales T, Domack M, Wagner J. Mater Sci Forum 2006;519–521:1585.
[77] Hirsch J, Lücke K. Acta Metall 1988;36:2863.